Supporting information

Ion Write Micro-Thermotics: Programing Thermal Metamaterials at the Microscale

Hwan Sung Choe[1,2†], Radhika Prabhakar[3†], Geoff Wehmeyer[4†], Frances I. Allen[1], Woochul Lee[2,5], Lei Jin[1,2], Ying Li[6], Peidong Yang[2, 5], Cheng-Wei Qiu[6], Chris Dames[2, 4], Mary Scott[1, 7], Andrew Minor[1, 7], Je-Hyeong Bahk[3*], Junqiao Wu[1,2*]

[1] *Department of Materials Science and Engineering, University of California, Berkeley, California 94720, USA*

[2] *Materials Sciences Division, Lawrence Berkeley National Laboratory, Berkeley, California 94720, USA*

[3] *Department of Electrical Engineering and Computer Science, University of Cincinnati, Cincinnati, Ohio 45221, USA*

[4] *Department of Mechanical Engineering, University of California, Berkeley, California 94720, USA*

[5] *Department of Chemistry, University of California, Berkeley, California 94720, USA*

[6] *Department of Electrical and Computer Engineering, National University of Singapore, Singapore, 117583*

[7] *The Molecular Foundry, Lawrence Berkeley National Laboratory, Berkeley, California 94720, USA*

[†] These authors contributed equally to this work.

*Authors to whom correspondence should be addressed, Electronic addresses:

wuj@berkeley.edu and bahkjg@ucmail.uc.edu

Thermal conductivity modelling.

We model the thermal conductivity of silicon using the kinetic theory result $\boldsymbol{\kappa} = \frac{1}{3}\sum_p \int C_{\omega,p} v_{\omega,p} \Lambda_{\omega,p} d\omega$, where $\boldsymbol{p}$ indexes the phonon polarization, $\boldsymbol{\omega}$ is the phonon frequency, $C_{\omega,p}$ is the volumetric modewise specific heat, $v_{\omega,p}$ is the group velocity, $\Lambda_{\omega,p} = v_{\omega,p}\tau_{\omega,p}$ is the mean free path, and $\tau_{\omega,p}$ is the scattering time. This expression for $\boldsymbol{\kappa}$ assumes that the phonon dispersion relation and scattering rates are isotropic, an assumption which is commonly employed when modeling thermally isotropic materials such as silicon.

We use the Born-von Karman isotropic approximation for the silicon phonon dispersion relation $\omega = \omega_0 \sin\left(\frac{2k}{\pi k_0}\right)$, where $\boldsymbol{k}$ is the phonon wavevector, $k_0 = (6\pi^2\eta_{PUC})^{1/3}$ is the Debye cutoff wavevector fixed by the experimental primitive unit cell density $\eta_{PUC} = 2.5 * 10^{23}\ \mathrm{m}^{-3}$ [1], and $\omega_0 = 2v_s k_0/\pi$ is fixed by the experimental speed of sound v_s. We obtain v_s by an unweighted averaged of the measured speeds of sound along the [100], [110], and [111] directions and obtain $v_{s,LA} = 8973\ \mathrm{m/s}$ for the longitudinal polarization and $v_{s,TA} = 5398\ \mathrm{m/s}$ for the two transverse polarizations [1].

We use Matthiessen's rule to combine the phonon-phonon (Umklapp) scattering rate τ_U^{-1}, boundary scattering rate τ_B^{-1}, and impurity scattering rate τ_I^{-1} as $\tau^{-1} = \tau_U^{-1} + \tau_B^{-1} + \tau_I^{-1}$. To model the phonon-phonon scattering, we use the relation $\tau_U^{-1} = P\omega^2 T \exp(-C_U/T)$ with the values $P = 1.9 * 10^{-19}\ \mathrm{s.K}$ and $C_U = 280\ \mathrm{K}$, which were obtained by a fit to temperature-dependent $\boldsymbol{\kappa}$ measurements of bulk silicon [2]. The film thickness and nanoribbon aspect ratio are used to calculate the boundary scattering mean free path for a rectangular nanowire assuming fully diffuse boundary scattering [3, 4]. The form of the impurity scattering rate is $\boldsymbol{\tau_I^{-1}} = \boldsymbol{A\omega^4}$: for the bulk sample, $\boldsymbol{A = 2.5 * 10^{-45}\ s^3}$ .We obtain the impurity scattering strength $\boldsymbol{A}$ for each sample by fitting the measured $\boldsymbol{\kappa(T)}$. We note here that $\boldsymbol{A}$ is the only free fitting parameter in the model.

Suppplementary Table 1 shows the values of the impurity scattering strength parameter $\boldsymbol{A}$ as a function of the ion dose. Here, $\boldsymbol{A}$ was determined by fitting to the data shown in Fig 2 of the main text. $\boldsymbol{A}$ increases monotonically with ion dose, representing the enhanced scattering with increasing point defect concentration. Supplementary Table 2 shows the values of $\boldsymbol{A}$ used in the reversibility studies of Fig. 4a,b.

Dose (ions/cm^2)	Pristine	2×10^{13}	1×10^{14}	1×10^{15}	1×10^{16}	1×10^{17}	1×10^{18}
Impurity parameter $\boldsymbol{A}$ (10^{-45} s^3)	5.3	8.5	19	59	190	910	5500

Supplementary Table 1: Impurity scattering parameters as a function of ion dose used in thermal conductivity modeling in Fig. 2. A is the only free fitting parameter in the model.

Dose (ions/cm^2)	1×10^{14}	1×10^{15}
Pristine impurity parameter $\boldsymbol{A}$ (10^{-45} s^3)	5.5	4.8
Irradiated impurity parameter $\boldsymbol{A}$ (10^{-45} s^3)	14	67
Annealed impurity parameter $\boldsymbol{A}$ (10^{-45} s^3)	7	13.5

Supplementary Table 2: Impurity scattering parameters for pristine, irradiated, and annealed samples shown in Fig. 4.

SRIM simulation of ion irradiation.

Monte Carlo simulations were performed using the stopping and range of ions in matter (SRIM) and the transport of ions in matter (TRIM) programs [5] to evaluate and predict the lattice damage of the 25 keV He$^+$ ion irradiation into the 120-nm-thick Si membrane. Considering the spot size (~1 nm) of the focused He$^+$ ion beam, the irradiation dose was calculated by the accumulated number of incident ions. The simulation results listed in Table S3 and S4 and Figure S1 show that, (1) most of (> 99%) the incident He$^+$ ions penetrate through the entire thickness of the suspended Si membrane without chemically doping the material, and (2) the defects introduced by the ion irradiation distribute reasonably uniformly across the thickness of the membrane. These SRIM and TRIM simulations indicate that the 25keV He$^+$ ion writing has a lateral resolution that depends on both the film thickness and the irradiation dose, ranging from 10 nm (for low doses < ~ 10^{15} ions/cm^2) to ~100 nm (for high doses ~ 10^{18} ions/cm^2) for the 120-nm-thick Si membrane.

Irradiation dose (ions / cm^2)	Si vacancies / He ion	Backscattered He ions	Transmitted He ions
10^{16}	19.1	1.0%	99.0%
10^{17}	23.8	1.3%	98.7%
10^{18}	23.1	1.4%	98.6%

Supplementary Table 3: Simulated number of Si vacancies created per incident helium ion, and the percentage of backscattered and transmitted He^+ ions through the 120 nm-thick Si membrane. They add up to 100.0%, meaning that a negligible percentage of the He^+ ions stay embedded in the Si membrane.

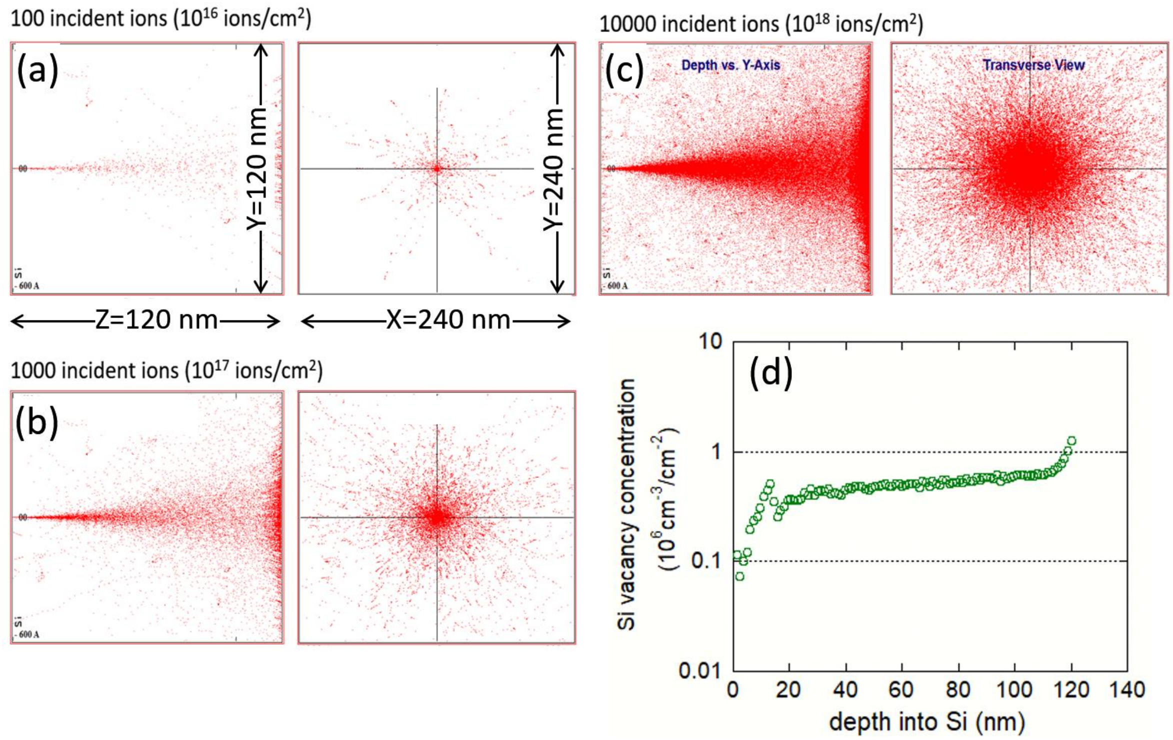

Figure S1: (a) – (c), SRIM simulated lattice damage when the 25keV He^+ ions are focused onto a single spot (< 1 nm) at a dose of 10^{16}, 10^{17} and 10^{18} ions/cm^2, respectively. The entire area shown is 120 nm × 120 nm for the longitudinal Y-Z plane (left panel) and 240 nm × 240 nm for the transverse X-Y plane at the back surface of the membrane (right panel). It can be seen that the lateral scattering of damage ranges from ~ 10nm to ~ 100nm depending on the dose, which defines the spatial resolution for the ion writing. (d) When the focused ion beam is rastered over the sample for laterally uniform irradiation, the simulated vacancies generated distribute reasonably uniformly over the membrane thickness. Here the vacancy concentration is given in cm^{-3}/cm^{-2}, meaning that the real vacancy concentration (in vacancies/cm^3) is this number multiplied by the irradiation dose (in ions/cm^2).

Thermoreflectance imaging (TRI) operation

The operation of the thermoreflectance imaging setup is briefly explained as follows.

The device under test (DUT) was biased for a certain time period and duty cycle. The LED light pulses were offset by a specific time delay relative to the device excitation. The CCD camera, exposure time of which was set up according to the device excitation, captured the reflected LED light from the device, thus storing reflected light variations from the hot and cold surfaces. Refer to Figure S2 for the timing diagram for this experiment. The system took a reference image at the LED delay of $t = 0$ with respect to the device excitation, which was used for image registration, alignment of the $t > 0$ images, and also for controlling the piezo stage for the xy and z drifts to prevent any long term drifting of the sample. Details of this setup and alignment procedures can be found in Reference [6].

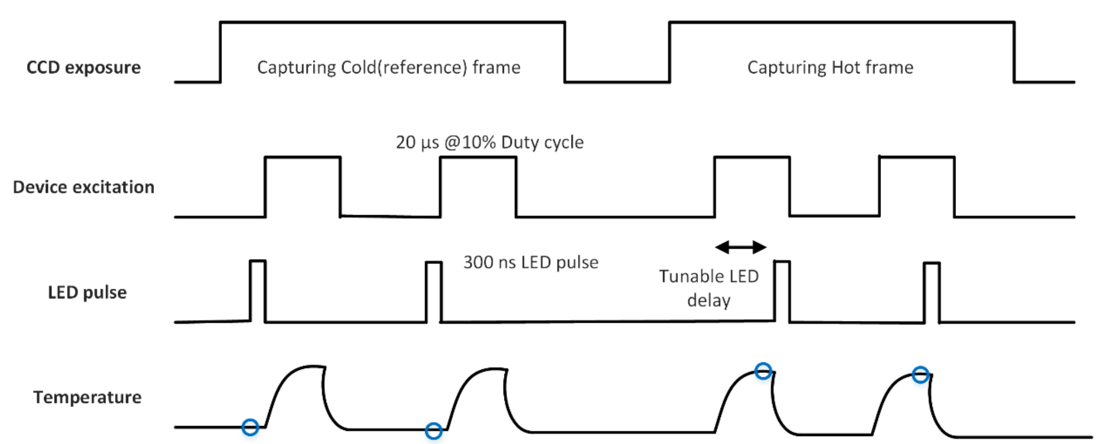

Figure S2: Timing diagram for capture of the reference (cold) image and the hot image. For our measurements, we used a 20 µs voltage pulse to bias the heaters and 300 ns LED pulse for illumination. Blue circles show that the cold (reference) image was taken just before the device was turned ON, and the hot image was taken when the device reached steady state temperature after being powered ON. The CCD exposure time was adjusted to capture both the hot and cold images.

Thermoreflectance coefficient (C_{tr}) calibration and temperature mapping.

C_{tr} calibration is done as a two-step process. First, steady state measurements are used for determining a single-value reference C_{tr} on a substrate supported material. Second, transient measurements, along with the reference C_{tr}, are used for obtaining a C_{tr} map on the suspended Si membrane. Thermal images are then taken at steady state temperatures and combined with the C_{tr} map to obtain the temperature distribution on the membrane.

Substrate supported devices with microscale features and larger allow simple global heating of device carrier / substrate while observing the temperature to obtain a C_{tr} map. Using a thermoelectric module or a heating stage, the device carrier is cycled between high and ambient temperatures to obtain the varying intensity 'hot' and 'cold' CCD frames.

For suspended MEMS devices, however, such a method for calibration is often not possible for the following reasons. First, isothermal heating of the device carrier does not allow for accurate temperature measurement on the membrane. The smallest thermocouples are 13-50 µm in size [7], using them for temperature measurement on the suspended heater pads or membrane is not possible due to the fragile nature of the device. Second, even if we somehow manage to measure the temperature *in situ*, there will be considerable edge effect artifacts caused by global thermal expansion. Global thermal expansion gains considerable importance at larger magnifications and when the feature sizes are in the sub-micron range. There is a considerable expansion of the heating stage and the thermal expansion of the sample interferes with the piezo stage corrections, thus leading to drifts and artifacts [6]. The smallest feature (ring linewidth) size in these devices is 500nm and 250nm for the bilayer and quadlayer metamaterial membrane, respectively. In such a case, local heating of the sample in question is most accurate.

We use the suspended heater pads for local heating of the Si membrane, with transient calibration technique [6], which involves capturing of a series of thermoreflectance images of device cooling after it reaches a peak temperature and is turned off. However, as will be seen in the description of this method below, the transient calibration method does need a reference C_{tr} for determining ΔT and extraction of C_{tr} map. We determine the C_{tr} of a Pt contact pad on the chip, which is substrate supported by steady state global heating. This is used to extract the (single-value) C_{tr} of the SiN_x on the suspended heater. We use this as the reference C_{tr} for extracting the thermal cloak map. SiN_x, which is present as a larger rectangular area on the heater pad, is better suited for use with the *TransientCAL* method than the narrower serpentine Pt pattern (see Fig. S3a). The SiN_x C_{tr} value obtained by cycling the device on substrate between high and low temperatures was -5.0×10^{-4} K^{-1}.

Figure S3(a) shows the CCD image of the Si membrane and the heaters. For local heating, and to observe the thermal decay via transient thermoreflectance imaging, both heaters were equally biased to uniformly heat the membrane using a 20 μs (2% duty cycle) voltage pulse. The thermal cloak thus reached its peak temperature at 20 μs and began to cool subsequently. Using a larger duration pulse, for instance, 100 μs to ~1ms, led to large amount of heating of the suspended device, causing twisting and bending of the suspension, thus affecting the focus and reflectance data. We therefore used small duration pulse at 2% - 20% duty cycle to avoid overheating and allow for enough cooling time. We collected ~14 transient thermoreflectance images from ~20 μs to 670 μs separated by a time interval of 40 μs. Each image was averaged for 1000 seconds to minimize the noise.

Two SiN_x regions (blue and red regions on the heater in Figure S3(a)) were selected on the micro heaters to be used as reference microscale structures for the transient calibration. ΔT for these regions was ascertained by the reference C_{tr} value obtained above (-5.0×10^{-4} K^{-1}). The transient cooling temperatures for these regions can be seen in Fig. S4 (a). It can be seen that ΔT of these regions approached zero in a few hundred microseconds after the heaters are turned off. This is as expected and we used this value for transient calibration.

Assuming uniform heating of the suspended heaters and the Si membrane, this ΔT was used as a reference to determine the thermoreflectance coefficients on a pixel by pixel basis thus obtaining a C_{tr} map of the Si membrane using the *TransientCAL* method. Figure S3(b) shows the C_{tr} map of the membrane thus obtained.

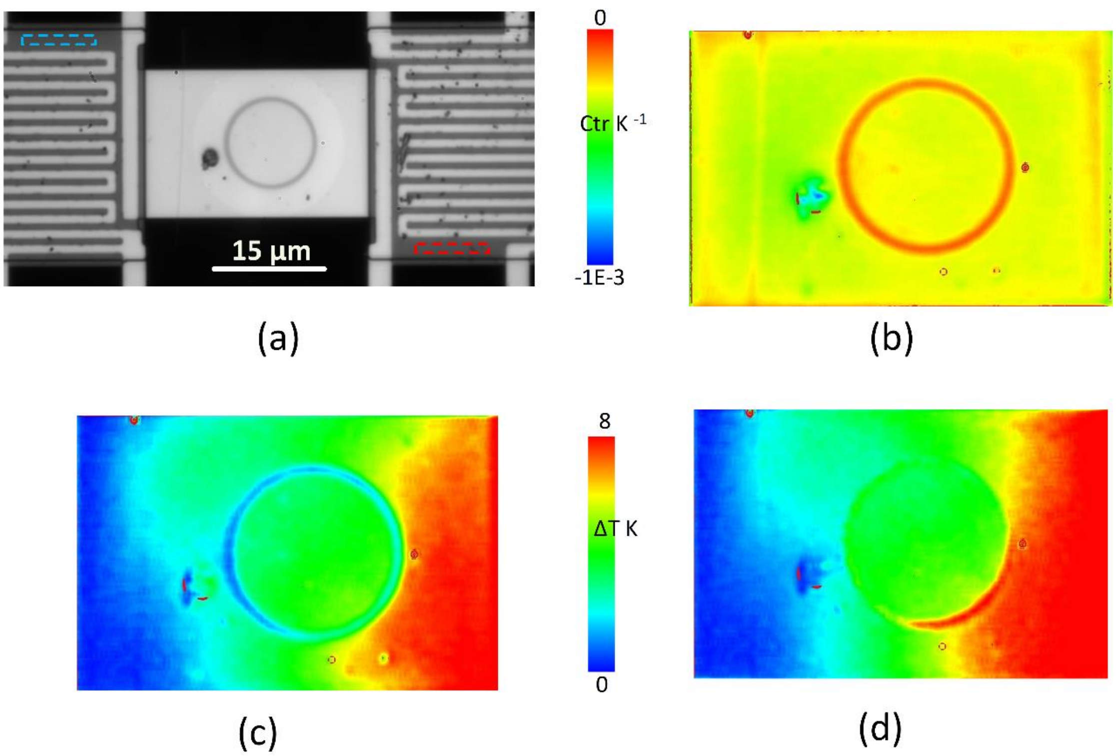

Figure S3: (a) CCD image of the suspended metamaterial Si membrane with the heaters. The dashed red and blue boxes show the SiN_x region, the ΔT of which was used as a reference for the transient calibration. (b) C_{tr} map obtained from the transient calibration method. (c) Raw thermoreflectance signal from the membrane when heating the right side (here the average Si C_{tr} is applied to obtain the ΔT), and (d) the actual temperature obtained on the surface of the membrane after application of the C_{tr} map. It can be seen that application of the C_{tr} map corrects for artifacts obtained on submicron features leading to more accurate temperature information, and one C_{tr} cannot be used for the complete membrane, reaffirming the need for a pixel-by-pixel C_{tr} calibration.

Next, thermal characterization of the metamaterial membrane at steady state temperature was done by turning on one of the heaters to observe the heat flow across the membrane. Thermal images were taken at 20 µs (at 10% duty cycle) when the devices reached their peak temperature (as shown by the simulation in Fig.S4(b)). A longer time averaging (~3600 seconds) was used for the capture of the data to reduce the noise. The raw thermoreflectance data is plotted in Figure S3(c), whereas (d) shows the actual temperature map after application of the C_{tr}.

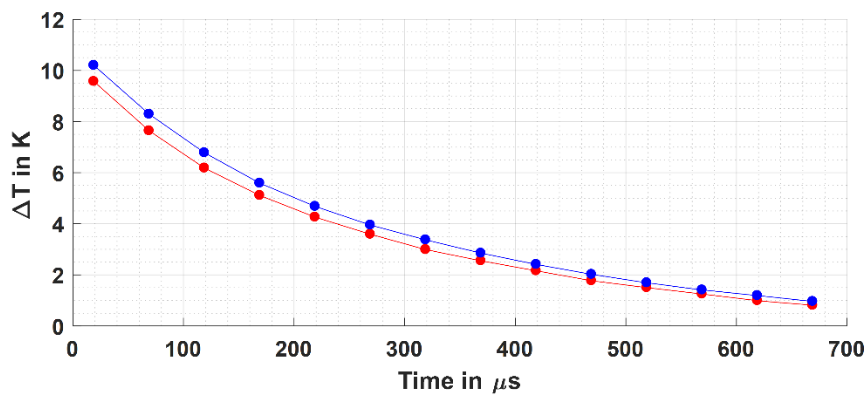

(a)

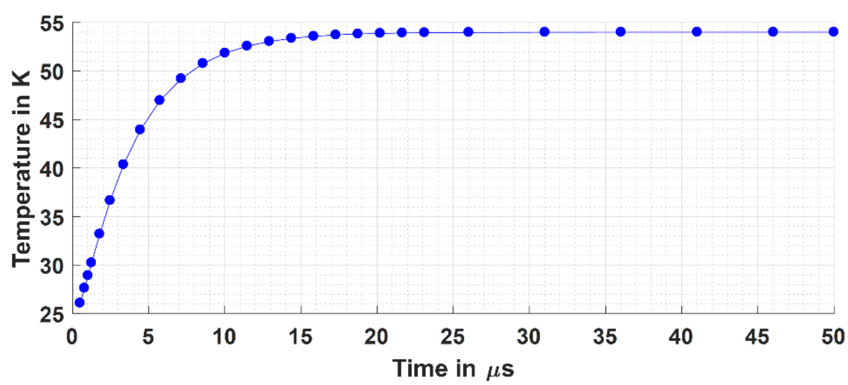

(b)

Figure S4: (a) Measured cooling of the left (blue) and right (red) SiN_x regions on the heater pad. They were heated for 20 µs and then turned off. The highest temperature can be seen at ~19 µs when the heater is ON, followed by subsequent cooling with the lowest ΔT ~ 669 µs. These temperatures were recorded using transient thermoreflectance imaging. (b) Simulation for the Si bilayer cloak shows that the device reaches a peak steady state temperature at ~20 µs. The FEM simulations were done in ANSYS for the device shown in Fig. 1b using the thermal conductivities of 2, 40, 70 W/m-K. This heating time was also used for measurements of the quadlayer cloak.

TRI measurement uncertainty discussion

To ensure high signal-to-noise ratios, TRI measurements are averaged over time, with typical averaging times being ~30 minutes or more. These long averaging times reduce the standard error of the measurement due to random noise to ~0.1K, as stated by TRI system specifications, and is similar to previous TRI measurements of bulk samples. Although this random error is appealingly small, averaging cannot eliminate potential uncertainties due to systematic errors or offsets (i.e. in general, measurements can be precise without necessarily being accurate). Surface roughness is one such systematic error source for TRI measurements [8]. Another potential source of error is device tilting. We now discuss the steps taken to minimize these potential systematic errors.

Surface roughness can affect the thermoreflectance coefficient because the incident light is not scattered specularly from the surface. To reduce the error due to surface roughness in the calibrations, the (single-value) calibration thermoreflectance coefficients C_{tr} of the SiN and the Pt pads are averaged over the largest possible pixel area available within the material analyzed. Care is taken to avoid edges and defects while selecting this averaging area. For the thermal cloak, a C_{tr} map is extracted using the transient calibration method and used with the reflectance map to obtain a pixel by pixel temperature map, fully accounting for non-uniformities in the thermoreflectance coefficient on the thermal cloak.

Another potential source of error is non-uniformity in the measurement of reflected light due to device tilts. To reduce this tilting effect, it is ensured that the TRI stage holding the device under test is levelled and isolated from vibrations. In addition, the TRI system used for these measurements includes piezo stages and auto focus to enable adjustments in case of device tilting and movement for small distances (~ 1 μm) and angles (~2 degrees). Furthermore, using local heating of the membrane for transient calibration reduces the impact of thermal expansion related effects, which are commonly seen for global heating calibrations and could potentially lead to drifts and artifacts.

Lastly, as discussed in the manuscript, the TRI images in Fig. 3 display noticeable asymmetries. Similar asymmetries were observed in TRI images of other thermal cloaks that we fabricated, and this temperature asymmetry was also seen in the same pristine device before patterning of the cloak (indicating that the cloak patterning process did not introduce the asymmetry). However, no asymmetries were observed in control TRI experiments for pristine devices which were supported on substrates (rather than being released and suspended), or on previous measurements for bulk samples. These control experiments indicate that the origin of the asymmetries could be due to the non-uniform thickness of the membrane (introduced before the cloak patterning), or due to non-uniform thermal tilts and built-in strains arising from the membrane release process. However, there might be other sources that contribute to the asymmetry as well, which warrants further investigation when studying temperature mapping of suspended membranes.

Verifying validity of thermal conductivity measurement

The underlying analytical model for extracting the device thermal conductance $\boldsymbol{G}$ from the measured data assumes that both the micro-heater and the sensor pads are isothermal. Of course, because heat is flowing from the pad to the sample, the pad can never be completely isothermal; however, if the device thermal resistance is sufficiently large, then the majority of the temperature drop occurs over the device, (rather than inside the pad), and the approximation is valid. In our experiments, the worst-case deviation from this idealized case would occur for the pristine device, which has a thermal resistance of $\boldsymbol{R}_{\mathbf{dev}} = \frac{L}{\kappa w t} = \mathbf{1.2} * \mathbf{10^6}\,\frac{\mathrm{K}}{\mathrm{W}}$, where $\boldsymbol{L} = \mathbf{20\mu m}$ is the device length, $\boldsymbol{w} = \mathbf{2\ \mu m}$ is the device width, $\boldsymbol{t} = \mathbf{120\ nm}$ is the device thickness, and $\boldsymbol{\kappa} = \mathbf{67}\,\frac{\mathrm{W}}{\mathrm{mK}}$ is the pristine conductivity at room temperature. We estimate the thermal resistance due to heat flow constriction from the pad into the device to be $\boldsymbol{R}_{\mathbf{pad-device}} = \mathbf{9.2} * \mathbf{10^4}\,\frac{\mathrm{K}}{\mathrm{W}}$; this estimate was obtained using an analytical solution for the constriction resistance between two rectangular channels with equal $\boldsymbol{\kappa}$ (Eq. 3.140 in Ref .[9]) for the case where the constriction ratio is equal to $\frac{w}{w_{\mathrm{pad}}}$, where $\boldsymbol{w}_{\mathbf{pad}} = \mathbf{30\ \mu m}$ is the pad width. This $\boldsymbol{R}_{\mathbf{pad-device}}$ estimate is conservative because it considers only heat transfer through the monolithic silicon portion of the pad, neglecting the parallel heat flow pathways through the SiNx and Pt on top of the pad, which would further reduce the thermal resistance of the pad. Therefore this analysis indicates that because the device thermal resistance $\boldsymbol{R}_{\mathbf{dev}}$ is at least an order of magnitude larger than the spreading resistance $\boldsymbol{R}_{\mathbf{pad-device}}$ in all cases, the isothermal pad approximation is reasonable. This conclusion is further supported by the good agreement between the measured pristine $\boldsymbol{\kappa}$ and previous silicon thin film measurements [10].

Demonstration of thermal rectification with IWMT

Thermal rectification, which occurs when heat flow experiences higher resistance in one direction than in the opposite direction, can be realized in a device called a thermal diode. Thermal diodes can find application, for example, in solid-state refrigeration cycle utilizing the magnetocaloric or electrocaloric effect. The thermal diode allows for strong thermal coupling when heat is pumped out of the refrigerator, while partially blocking undesirable heat backflow into the refrigerator during other portions of the cycle [11]. One way to realize the thermal rectification is a "junction thermal diode”, consisting of two segments with $\kappa(T)$ that have very different temperature trends [12, 13]. According to Ref.[13], in the ideal case when the thermal resistances of the left and the right segments are matched, and if their thermal conductivities depend on temperature as $\boldsymbol{\kappa_L(T) \propto T^{n_L}}$ and $\boldsymbol{\kappa_R(T) \propto T^{n_R}}$, it is expected that the thermal rectification is proportional to the temperature bias as $\boldsymbol{\gamma = \frac{(n_L - n_R)}{4}\Delta}$. Here $\boldsymbol{\gamma = \frac{Q_{LR} - Q_{RL}}{Q_{LR}}}$ is the thermal rectification, and $\boldsymbol{\Delta = \frac{T_H - T_C}{\frac{1}{2}(T_H + T_C)}}$ is dimensionless thermal bias. In these equations, the subscription “L” and “R” stand for the left- and the right-hand side, respectively, and “H” and “C” stand for the hot and cold side, respectively.

The Si membrane in the IWMT can be irradiated with different doses to form a junction thermal diode. As shown in Fig. S5(b), the membrane was irradiated in the two segments with 10^{14} and 10^{18} ions/cm^2 doses, which provided a ratio in κ of 28.5 at 200 K. For maximal thermal rectification, the length ratio of the two segments was set also at 28.5. A thermal rectification ratio of 2.4% was observed at 200K with 30K temperature bias of the device, as shown in Fig. S5(c). Fitting of the data in Figure S5(c) and (d) yields $\boldsymbol{\gamma = 0.16\,\Delta}$.

The $\kappa(T)$ data in Fig.S5(a) gives best-fit temperature dependence of $\boldsymbol{\kappa_L(T) \propto T^{-0.37}}$ and $\boldsymbol{\kappa_R(T) \propto T^{0.24}}$ near 200 K. Hence, a relationship of $\boldsymbol{\gamma = 0.15\,\Delta}$ is expected. This is in good agreement with the experimental data in Fig.S5(e).

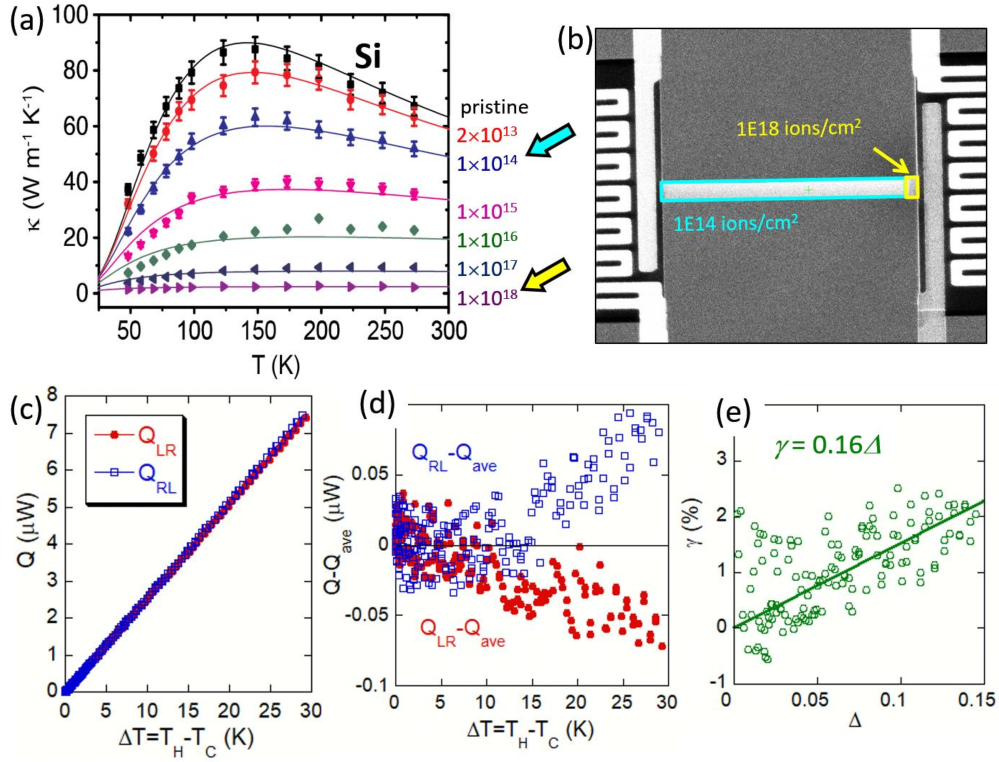

Figure S5: A thermal diode created by selective He^+ ion irradiation. (a) Thermal conductivity of the Si membrane as a function of temperature for various irradiation doses. Arrows show the two doses that are used for irradiation in the diode demonstration. (b) SEM image of the selectively irradidated Si membrane creating two segments of 10^{14} and 10^{18} ions/cm^2 doses, respectively. The membrane is 30 μm long and 2.3 μm wide. (c) Heat flow through the device (Q) as a function of temperature bias (ΔT) at a base temperature of 200 K. Blue (red) data points correspond to the case of heat flow direction from right (left) to left (right). (d) The heat flow asymmetry Q-Q_{ave} plotted as a function of ΔT, where $Q_{\mathrm{ave}} = (Q_{\mathrm{LR}}+Q_{\mathrm{RL}})/2$ is the averaged heat flow. (e) Experimentally measured thermal rectification (γ) as a function of dimensionless thermal bias (Δ). The line is a linear fit, which yields $\gamma = 0.16\Delta$, in good agreement with the theoretical prediction of $\gamma = 0.15\Delta$.

Experimental heat flux mapping in the thermal cloaks

Thermal cloaks route heat flow away from the cloaked object, meaning that the magnitude of the heat flux should be much larger in the cloak region than within the central cloaked object. We illustrate this heat flux routing using our experimental TRI temperature map $T(x, y)$ to obtain a local heat flux map $q_x(x, y)$. First, we smooth the TRI $T(x, y)$ image before evaluating $\frac{dT}{dx}$ numerically using a central-difference method. Smoothing the data by taking a moving average of the temperature profile over a square 600 by 600 nm averaging window reduces the variation in $\frac{dT}{dx}$ due to experimental noise. To obtain $\kappa(x, y)$ for regions (i), (ii) and (iii), we use our experimentally measured values of κ for uniformly irradiated silicon membranes of the same film thickness and dose. We then obtain the x-direction heat flux $q_x(x, y)$ using Fourier's law, $q_x = -\kappa \frac{dT}{dx}$.

In Fig. 3 of the main text, we plot the magnitude $|q_x(x, y)|$ over a limited range of values to emphasize the difference between the heat flux in the central object and in the pristine regions of the cloak. The clipped values of $|q_x(x, y)|$ which are larger than the upper range of the color map are represented in gray rather than in color. Most of these clipped regions have large values of $|q_x(x, y)|$ due to experimental artifacts from contamination or from the TRI temperature measurements within the heavily irradiated region (iii). We chose to plot the magnitude of the x-component of the heat flux q_x in Fig. 3, rather than the magnitude of the total heat flux $q = \|\kappa \nabla T\|$ because we found that q_x was less sensitive than q to edge effects in the numerical derivative near the edges of the suspended membrane.

Quadlayer thermal cloak simulations

In addition to the bilayer cloak shown in Fig. 2a and Fig. 2b, we also designed a quadlayer cloak with two separate irradiated regions. The experimental results for the temperature and heat flux are shown in Fig. 3c, and the numerical predictions are shown in Fig. S6. For this device, $L = 30$ µm, $w = 25$ µm, and the radius of the inner region is 6.9 µm. The radial width of each irradiated region is 350 nm, and the thickness of each pristine region is 2.45 µm.

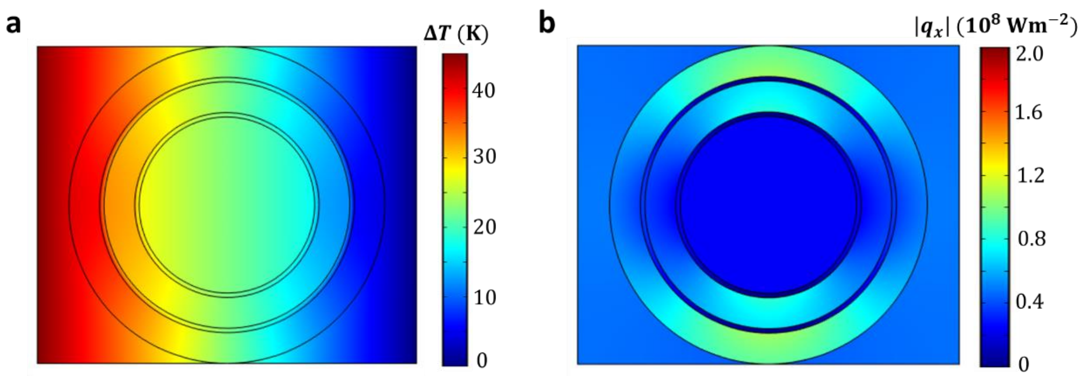

Figure S6: Simulated (a) temperature profile and (b) heat flux $\boldsymbol{q_x}$ maps for the quadlayer cloak.

Negligible heat flux in the cloaked region at different levels of total heat flux

We applied different heat fluxes to the quadlayer thermal cloak, and observed the temperature maps using TRI. Figure S7 shows that with increase in temperature bias, the heat flux through the membrane increases, but the temperature gradient in the cloaked region remains nearly the same, proving the thermal cloaking capability of the device.

The temperature vs. position linecut in Fig S7 shows dips in temperature profile in and around the high irradiation intensity rings due to artifacts. With the dimensions of the the rings being close to diffraction limits (TRI measurements use blue light of λ= 470 nm and the thickness of the rings for the quadlayer device is ~250 nm), edge effects from these features and their boundaries lead to incorrect temperature estimation at these regions. In the absence of these artifacts, the black dashed lines would indicate a close estimation to the temperature gradient on the highly irradiated regions.

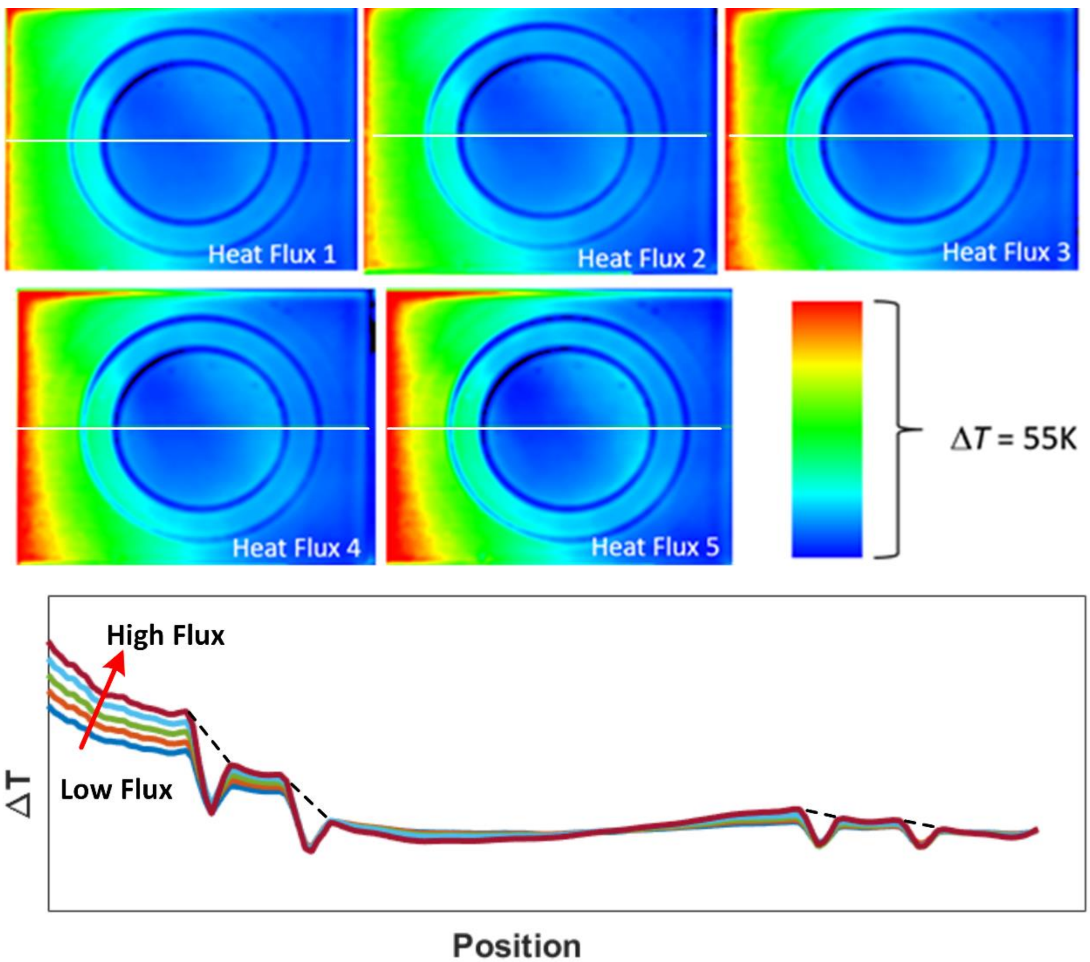

Figure S7: Temperature map of a quadlayer cloak at different heat flux (by increasing temperature bias). It can be seen that although the total heat flux and temperature bias are increased, the temperature linecut in the cloaked region remains flat. This indicates that the heat flux in the region is nearly zero and insensitive to the imposed thermal gradient, which proves the function of thermal cloaking. The dips in the temperature profile on either side of the central region are artifacts due to edge effects at the boundaries at regions of high irradiation intensity, where the TRI signal is not reliable. The black dashed lines have been drawn to show what would be a close estimation of temperature profile in absence of the artifacts on and around high irradiation intensity rings.

Supplementary information references

[1] Dames C.; Chen, G., J. Appl. Phys. 2004, 95, 682.

[2] Yang, F.; Dames, C., Phys. Rev. B, 2013, 87, 035437.

[3] McCurdy, A. K.; Maris, H. J.; Elbaum, C., Phys. Rev. B, 1970, 2, 4077.

[4] Lee, Jaeho; Lee, Woochul; Wehmeyer, Geoff; Dhuey, Scott; Olynick, Deirdre L.; Cabrini, Stefano; Dames, Chris; Urban, Jeffrey J.; Yang, Peidong. Nature Commun. 2017, 8, 14054.

[5] The Stopping and Range of Ions in Matter, http://www.srim.org/

[6] Kendig, D.; Hohensee, G.; Pek, E.; Kuang, W.; Yazawa, K.; Shakouri, A.; in 16th IEEE Intersociety Conference on Thermal and Thermomechanical Phenomena in Electronic Systems (ITherm), 2017, 23.

[7] Christofferson, J.; Maize, K.; Ezzahri, Y.; Shabani, J.; Wang X.; Shakouri, A., Journal of Electronic Packaging, 2008, 130, 041101.

[8] D. Kendig, et al., in 28th Annual IEEE Semiconductor Thermal Measurement and Management Symposium (SEMI-THERM). IEEE, 2012.

[9] Yovanovich, M. M., in *Handbook of Heat Transfer*, edited by Rohsenow, W. M.; Hartnett, J. P.; Cho, Y. L.; McGraw–Hill, New York, 1998, Chap. 3.

[10] Marconnet, A. M.; Asheghi, M.; Goodson, K. E.; J. Heat Transfer, 2013, 135 (6), 061601.

[11] Wehmeyer, G.; Monachon, C.; Yabuki, T.; Wu J.; Dames, C.; Appl. Phys. Rev., 2017, 4, 041304.

[12] Heinrich Hoff, Physica, 1985, 131A, 449.

[13] Dames, C., J. Heat Transfer, 2009, 131, 061301.